

See discussions, stats, and author profiles for this publication at: <https://www.researchgate.net/publication/276835654>

Effects of Critical Fluctuations on Adsorption-Induced Deformation of Microporous Carbons

ARTICLE *in* THE JOURNAL OF PHYSICAL CHEMISTRY C · MARCH 2015

Impact Factor: 4.77 · DOI: 10.1021/acs.jpcc.5b00226

READS

41

5 AUTHORS, INCLUDING:



A. Ciach

Instytut Chemii Fizycznej PAN

105 PUBLICATIONS 1,026 CITATIONS

[SEE PROFILE](#)



Piotr A Gauden

Nicolaus Copernicus University

224 PUBLICATIONS 1,942 CITATIONS

[SEE PROFILE](#)

Effects of Critical Fluctuations on Adsorption-Induced Deformation of Microporous Carbons

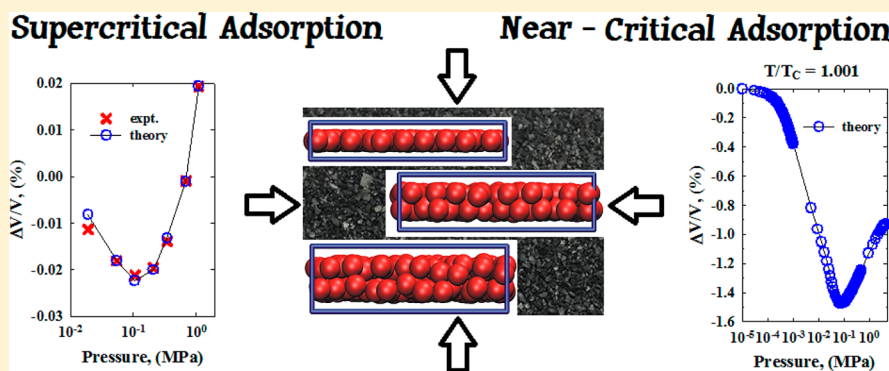
Piotr Kowalczyk,^{*,†} Alina Ciach,[‡] Artur P. Terzyk,[§] Piotr A. Gauden,[§] and Sylwester Furmaniak[§]

[†]School of Engineering and Information Technology, Murdoch University, Murdoch 6150 Western Australia, Australia

[‡]Institute of Physical Chemistry, Polish Academy of Sciences, 01-224 Warszawa, Poland

[§]Faculty of Chemistry, Physicochemistry of Carbon Materials Research Group, Nicolaus Copernicus University in Toruń, Gagarin Street 7, 87-100 Toruń, Poland

Supporting Information



ABSTRACT: We study adsorption-induced deformation of microporous carbons in the vicinity of the critical temperature of the adsorbed fluid for a range of subcritical pressures. The thermodynamic model (Kowalczyk, P.; Ciach, A.; Neimark A. *Langmuir* 2008, 24, 6603) coupled with molecular simulations and experimental dilatometric measurements at $T/T_c = 1.623$ (T and T_c denote experimental and critical temperature, respectively) is used for constructing dilatometric deformation curve at $T/T_c = 1.001$. We find that the initial contraction of a microporous carbon sample upon near-critical argon adsorption is ~ 1.5 vol % (~ 2 orders of magnitude higher than at $T/T_c = 1.623$). Large initial contraction of microporous carbon is a result of significantly higher solvation pressures in carbon micropores generated by the near-critical argon adsorption. In supermicropores and narrow mesopores (pore size $\sim 0.7\text{--}5.0$ nm) we observe a crossover between the oscillatory solvation force in thin pores, and the attractive thermodynamic Casimir force in pores of very large thickness. In the crossover regime, the oscillatory decay is superimposed on an attractive background, and the repulsion between the confining surfaces appears only when the pressure exceeds a certain value depending on the pore width. The attractive force in all pores exceeding a certain width can lead to a significant increase of the contraction of the sample containing supermicropores and narrow mesopores when the critical temperature is approached at sufficiently low subcritical pressure (~ 0.4 MPa in the case of argon).

1. INTRODUCTION

Understanding the mechanism of adsorption-induced deformation is crucial for applications of microporous materials in the fields of separation, catalysis, strategic gas capture/storage, solvent extraction, and drug delivery.^{1–13} Therefore, recently, both experimentalists and theoreticians have reignited interest in this phenomenon.^{1,4} It has been shown experimentally that guest molecules adsorbed in micropores (with pore size lower than 2 nm) cause a substantial stress in the microporous solid, leading to its contraction or expansion and sometimes to morphological transitions.^{1,4} Novel phenomenological and statistical thermodynamics approaches have been extensively used for the microscopic modeling of adsorption-induced deformation phenomena at subcritical and supercritical temperatures.^{1,2,6–8} However, both, experimental dilatometric studies and a rigorous theoretical description of adsorption-induced

phenomenon close to the critical temperature (T_c) of the adsorbed fluid are lacking.

Elucidation of the microscopic mechanism of adsorption-induced deformation close to T_c is crucial in particular for the development of strategic CO_2 capture and storage.^{14,15} Enhanced coal bed CH_4 recovery by CO_2 injection is one of the most promising methods developed toward long-term storage of CO_2 .¹⁴ Coal bed CH_4 is present in coal seams (typical microporous carbonaceous materials) at pressures between 3 and 30 MPa and temperatures between 30 and 100 °C. Therefore, the temperature and pressure of CO_2 injection can be very close to the critical temperature (i.e., 31.1 °C), and

Received: January 8, 2015

Revised: February 18, 2015

Published: February 26, 2015



the critical pressure (7.39 MPa), indicating near-critical conditions of CO₂ adsorption.¹⁴ Regeneration of porous adsorbents by the use of CO₂ (including: subcritical, near-critical, and supercritical temperatures) is yet another technological process that may be affected by the sample deformation.¹⁶ Here, supercritical and near-critical CO₂ (promoted as green solvent) is used for extraction of adsorbed molecules from the microporous carbons.¹⁶ If the temperature of CO₂ extraction is close to its critical temperature, the packing of CO₂ molecules in micropores is affected by critical fluctuations. Therefore, a near-critical CO₂ adsorption may potentially induce deformation of microporous carbons, a fascinating yet poorly understood phenomenon.

Fluid confined between parallel surfaces induces effective interaction between these surfaces, called solvation force or solvation pressure, if the separation between the surfaces is up to a few molecular diameters σ .^{17,18} The solvation force reflects packing effects of the molecules, and is attractive or repulsive, depending on the wall separation H . For increasing H , the solvation force exhibits oscillatory decay similar to the oscillatory decay of the pair correlation function. For separations between the confining surfaces much larger than σ , the packing effects become negligible in the supercritical fluid, and it induces no stress on the surfaces. In 1978 Fisher and de Gennes¹⁹ predicted that critical fluctuations in the confined critical fluid lead to effective interactions between the confining surfaces even when their separation is much larger than the molecular size. Close to the critical point large domains with excess or depletion of density occur in the bulk. Near a strongly adsorbing surface, a thick film with excess density is formed (critical adsorption). When the films adsorbed at two such surfaces overlap, an effective attraction between the surfaces occurs. This long-range force has universal features, and is termed thermodynamic Casimir force, to distinguish it from the short-range solvation force in noncritical fluids. Note that the Casimir force is attractive for any $H \gg \sigma$.

The theory of the universal Casimir force is very well established and verified experimentally for surfaces separated by distances $H \gg \sigma$.^{20–23} Much less is known about the interactions induced by the near-critical fluid on the surfaces separated by the distances of order of a few σ . This is because the Landau–Ginzburg–Wilson theory focuses on the universal aspects of the critical phenomena, and in this theory the microscopic length-scale structure is averaged or disregarded.²⁴ The microscopic structure is very well described away from the critical point by the density functional theory (DFT).^{25–27} However, the DFT is of a mean-field type and cannot properly describe the critical fluctuations.²⁵ Thus, an efficient theoretical approach that correctly takes into account both the microscopic structure and the critical fluctuations is lacking. On the other hand, in the materials of practical significance, the pores are thinner than 1 nm.^{28–30} Thus, the question of adsorption stress induced on the typical carbonaceous microporous material by the near-critical fluid remains open. This question is very important from a practical point of view, and will be addressed in the present work.

We will focus on two main questions in this article. The first one is a comparison of the deformation of microporous carbons induced by adsorption of near-critical and supercritical argon. This question is associated with the adsorption stress induced by near-critical argon on pores of widths thinner than 1 nm. The second goal is the investigation of the crossover between the alternating attraction and repulsion for $H \sim \sigma$, and the

purely attractive Casimir force for $H \gg \sigma$. The crossover is expected near the bulk critical point for pores of a thickness of a few up to a few tens of σ , when neither the packing effects nor the critical fluctuations are negligible. We shall study the solvation force as a function of H and as a function of pressure, and compare its qualitative features with the properties predicted theoretically for the scaling regime that corresponds to much larger H .

We perform grand canonical ensemble Monte Carlo (GCMC) computer simulations for argon confined in slit-shaped carbon pores for a range of subcritical pressures p . We use argon as model fluid because of its simplicity, availability of experimental dilatometric measurements at supercritical temperatures, and quality of force fields. Next we use the simulation results for the solvation/Casimir force for the individual slit-shaped pores, and determine the average adsorption stress in porous material composed of slit-shaped pores with a particular distribution of widths (surface area $S(H)$ d H of the pore widths between H and $H + dH$). Finally, requiring mechanical equilibrium between the average adsorption stress in the pores and the elastic stress of the material, we shall obtain the volumetric strain. The thermodynamic procedure outlined above has been introduced and successfully compared with experimental results for supercritical argon in ref 31. In this work we assume that the pore-size distribution and the elastic constant of the material are the same as those determined in ref 31. The main question is how the volumetric strain in the near-critical and supercritical argon differ from each other for the same microporous material and for the same range of experimentally relevant pressures. The dilatometric measurements are typically performed for $p < 0.5$ MPa and we focus mainly on such pressures.⁴

In section 2.1 we briefly review thermodynamic relations for fluid confined in a slit-shaped pore. In section 2.2 we discuss the properties of the Casimir force. Next, in section 2.3 we present the equations describing the adsorption-induced deformation of microporous carbons derived in ref 31 and used in our computations. Simulation details with description of force fields and molecular models are given in section 3. In section 4 we present our results. We determine the critical parameters in section 4.1, and compute the solvation force for slit-shaped pores of different widths in section 4.2. The predictions of dilatometric deformation curve for carbide-derived activated carbon immersed in near-critical argon are presented in section 4.3. Final conclusions are given in section 5.

2. THERMODYNAMIC RELATIONS

2.1. Fluid Confined in a Single Slit-Shaped Pore. A distribution of molecules confined by two parallel surfaces separated by the distance H is different than in a bulk sample of the same volume SH , where S is the area of each surface. As a consequence, for a given thermodynamic state, the grand thermodynamic potential in the slit-shaped pore, $\Omega(H)$, differs from the grand potential in the bulk sample of the same volume, $\Omega_{\text{bulk}}(H) = -pHS$. For $H^2 \ll S$, the excess grand potential per surface area of one wall,^{18,31}

$$\Delta\Omega(H)/S = \Omega(H)/S + pH \quad (1)$$

consists of the sum of the wall–fluid surface tensions and of the fluid-induced effective potential between the confining surfaces. The fluid-induced solvation force per surface area S (solvation pressure) is given by^{18,31}

$$f_s(H) = \frac{-\partial\Delta\Omega(H)/S}{\partial H} = -p + \sigma_s(H) \quad (2)$$

where

$$\sigma_s(H) = \frac{-\partial\Omega(H)/S}{\partial H} \quad (3)$$

In order to compute $\sigma_s(H)$ we first determine $\Omega(H)$ by using thermodynamic integration,³¹

$$\Omega(\mu) = \Omega(\mu_r) - \int_{\mu_r}^{\mu} N(\mu) d\mu \quad (4)$$

where for the given chemical potential the number of molecules, $N(\mu)$ in the slit-shaped pore can be obtained from the GCMC simulations, and μ_r is the chemical potential in the reference system, for which $\Omega(\mu_r)$ is known. We choose as the reference system the ideal gas, and assume³¹

$$\Omega(\mu_r) = -k_B T N(\mu_r) \quad (5)$$

2.2. Properties of the Casimir Force. The solvation force defined in eq 3 is called Casimir force near the bulk critical point and for $H \gg \sigma$. This name reflects the universal properties. When temperature T and the chemical potential μ tend to their bulk critical values T_c and μ_c , respectively, i.e. $\tau \rightarrow 0$, $h \rightarrow 0$, where $\tau = (T - T_c)/T_c$ and $h = \mu - \mu_c$, then the solvation force between strongly adsorbing surfaces separated by a distance $H \gg \sigma$ takes the scaling form^{34,37}

$$f_c(H) = -k_B T \frac{A_c}{\zeta^3} \exp(-H/\zeta) F(\tau^{-(\beta+\gamma)} h) \quad (6)$$

where

$$\zeta = \zeta_0 |\tau|^{-\nu} \Xi_0(\tau^{-(\beta+\gamma)} h) \quad (7)$$

is the correlation length,^{24,32–34,36,37} F and Ξ_0 are scaling functions, k_B is the Boltzmann constant, the universal amplitude $A_c \approx 1.51$ was determined by simulations in ref 35 and verified in recent experiments,^{20,23} and ζ_0 is a fluid-dependent coefficient comparable with σ . Finally, $\nu = 0.63$, $\beta = 0.325$, and $\gamma = 1.237$ are the critical exponents for the gas–liquid critical point (Ising universality class). The scaling functions are both positive, and $F(0) = \Xi_0(0) = 1$. The above scaling or law of corresponding states means that the solvation force induced by various adsorbing fluids on attractive surfaces is the same (in $k_B T$ units) in thermodynamic states corresponding to the same values of $\tau^{-(\beta+\gamma)} h$ and ζ in each confined critical fluid. This law of corresponding states is valid only in the critical region and for $H \gg \sigma$.^{20,34,35}

In this work we are interested in pores that are not sufficiently thick, and the scaling behavior (i.e., eqs 6 and 7) is not expected to be valid. We want to compare the qualitative features of the universal Casimir force and the force induced by the near-critical fluid on the confining surfaces a few nanometers apart.

First of all, for large separations the near-critical fluid induces attraction between the surfaces separated by a distance much larger than the size of the molecules, $H > \zeta \gg \sigma$. Note that for H corresponding to geometrical compression of the confined atoms, repulsion occurs when H is not large. It is interesting for what values of H corresponding to geometrical compression of the confined atoms the repulsion is replaced by an attraction, and how it depends on pressure. We focus on this question in section 4.2.

Before describing the dependence of the Casimir force on $h = \mu - \mu_c$ for fixed H , let us note that the phase transition in confinement occurs in different thermodynamic states than in the bulk. The attractive surfaces induce a shift of the gas–liquid transition to smaller values of the chemical potential, $\mu_{coex}(H, T) < \mu_{coex}(\infty, T)$, where $\mu_{coex}(H, T)$ and $\mu_{coex}(\infty, T)$ denote the chemical potential at the gas–liquid coexistence in the slit-shaped pore and in the bulk, respectively. Simulations confirmed that according to Kelvin equation $\mu_{coex}(\infty, T) - \mu_{coex}(H, T) \propto 1/H$ for $H > 30\sigma$.³⁸ The gas–liquid coexistence in the slit-shaped pore (known also as capillary condensation) terminates at the critical point. The temperature at this critical point of the capillary condensation depends on H and is smaller than the critical temperature in the bulk. Thus, at the bulk critical temperature, the confined fluid is supercritical. It is important to note that in supercritical fluids some thermodynamic quantities assume maxima at the line, which is the extension of the coexistence line $\mu_{coex}(\infty, T)$ beyond the critical point.³⁹ In the case of the constant-pressure specific heat this line is called the Widom line.⁴⁰ One may expect that by analogy the Casimir force assumes an extremum for μ that lies at the extension of the coexistence line $\mu_{coex}(H, T)$ beyond the critical point of the capillary condensation. This means, in particular, that for $T = T_c$ the Casimir force should assume an extremum for $h < 0$.

Indeed, from theoretical results it follows that the magnitude of the Casimir force takes the maximum not for $h = \mu - \mu_c = 0$, but for some small negative value depending on H .⁴¹ Thus, for a given pore, the strongest stress is expected for a particular subcritical pressure, and this stress can be much larger than at the critical point.⁴¹ For increasing H , the absolute value of h corresponding to the maximum of the absolute value of the solvation force decreases. This is because for increasing H , the coexistence line and its extension in the slit-shaped pore approach the coexistence line and its extension in the bulk. We shall verify whether a similar dependence on pressure is found for wall separations on the order of a few nanometers in section 4.2.

2.3. Thermodynamic Model of Adsorption-Induced Deformation. We consider microporous material with isotropic distribution of slit-shaped pores, and assume that the pores of widths in the range $(H, H + dH)$ have the total area $S(H) dH$. We assume further that slit-shaped carbon pores are embedded in an incompressible matrix that transfers the adsorption stress isotropically (like the pressure in liquid).³¹ This assumption is justified by the fact that very high pressures are required to compress graphite, diamond, or mixed sp^2-sp^3 carbon phases.⁴² Furthermore, to the best of our knowledge, there are no experimental data on compressibility of carbide-derived carbon matrix (i.e., nonporous material with the same ratio of sp^2-sp^3 bonded carbon).⁴ Following Kowalczyk et al.,³¹ we assume that the average adsorption stress in the sample is given by

$$\bar{\sigma}_s = \frac{\int H \sigma_s(H, p) S(H) dH}{\int H S(H) dH} \quad (8)$$

Finally, we assume mechanical equilibrium between the average solvation (or excess) pressure in the pores, $\bar{\sigma}_s - p$, and the elastic stress of the microporous material, $K\varepsilon$. K denotes the bulk modulus, and $\varepsilon = \Delta V/V \approx 3\Delta L/L_0$ is the volumetric strain in the sample with the initial volume of $V_0 \approx L_0^3$. The mechanical equilibrium implies³¹

$$\varepsilon = \frac{1}{K} [\bar{\sigma}_s - p] \quad (9)$$

For small deformations, the volumetric strain ε of the microporous carbon can be obtained from the experimentally determined linear length change ΔL of the sample.

To the best of our knowledge, dilatometric measurements of adsorption-induced deformation of microporous carbons close to the critical point of the confined fluid have not been reported so far (see ref 4). Our goal here is a determination of the strain induced by the near-critical argon confined in pores of the carbon sample with the known microporoelastic properties (i.e., micropore size distribution and bulk modulus). The micropore size distribution and the bulk modulus for the sample studied by dilatometric experiments in ref 31 have been determined by fitting eq 9 to the experimental results, with $\sigma_s(H)$ computed from eqs 3–5 and the isotherms determined from the GCMC simulations for the supercritical argon with $T/T_c = 1.623$ in ref 31. We assume the same pore size distribution and the same bulk modulus for $T/T_c = 1.001$. To obtain from eqs 3–5 the adsorption stress in individual pores, $\sigma_s(H)$, we perform GCMC simulation for near-critical argon with $T/T_c = 1.001$.

3. SIMULATION METHODOLOGY

3.1. Interaction Potentials. We model the argon–argon interactions via the effective truncated (12,6) Lennard-Jones (LJ) potential:^{43,44}

$$U_{ff}(r) = 4\epsilon_{ff} \left[\left(\frac{\sigma_{ff}}{r} \right)^{12} - \left(\frac{\sigma_{ff}}{r} \right)^6 \right] \theta(r_{cut} - r) \quad (10)$$

Here, r is the distance between the two interacting argon atoms, σ_{ff} denotes the LJ collision diameter, ϵ_{ff} is the LJ well depth, $r_{cut} = 5\sigma_{ff}$ is the cutoff distance, and θ denotes the Heaviside function. The LJ parameters, $\sigma_{ff} = 0.3405$ nm and $\epsilon_{ff}/k_B = 119.8$ K, were previously fitted to argon properties in ref 44.

The total argon–carbon interaction potential is a superposition of the potentials exerted by the two opposing walls,⁴⁵

$$U_{sf}(z) = U_s(z) + U_s(H - z) \quad (11)$$

As in our previous study,³¹ the potential $U_s(x)$ is modeled by the 10-4 potential,⁴⁵

$$U_s(x) = 4\pi\rho_s\epsilon_{sf}\sigma_{sf}^2 \left[\frac{1}{5} \left(\frac{\sigma_{sf}}{x} \right)^{10} - \frac{1}{2} \left(\frac{\sigma_{sf}}{x} \right)^4 \right] \quad (12)$$

where $\rho_s = 38.2$ nm⁻² is the density of carbon atoms, σ_{sf} and ϵ_{sf} are the LJ solid–fluid collision diameter and the well depth, respectively. The parameters of the solid–fluid LJ potential were calculated from the Lorentz–Berthelot (LB) mixing rule: $\sigma_{sf} = (\sigma_{ff} + \sigma_{ss})/2$ and $\epsilon_{sf}/k_B = ((\epsilon_{ff}/k_B)(\epsilon_{ss}/k_B))^{1/2}$. For carbon we adopted the following parameters: $\sigma_{ss} = 0.34$ nm, and $\epsilon_{ss}/k_B = 28$ K. The experimental verification of the LB mixing rule for description of the noble gas-graphite system has been recently described.^{46,47}

3.2. Simulation Details. The liquid–vapor coexistence curve for argon was computed by our implementation of the Gibbs ensemble Monte Carlo simulation (GEMC).⁴⁸ We adopted the standard setup for the GEMC simulation, i.e., two cubic simulation boxes with periodic boundary conditions and minimum image convention for computing molecular interaction in the x , y , and z directions.^{48,49} Close-packed face-centered crystal (fcc) and gas consisting of randomly placed argon atoms were used as initial configurations in the GEMC

simulations. Phase equilibrium is achieved by using three Monte Carlo moves: particle displacement, particle exchange, and volume exchange.⁴⁸ In the particle displacement move, each box is independent. The probability of acceptance is the same as for conventional constant *NVT* simulations,⁴⁹

$$P_{dis} = \min[1, \exp(-\beta\Delta U)] \quad (13)$$

where $\beta = 1/k_B T$, and ΔU is the configuration energy change resulting from the displacement. This move creates energy fluctuations in each box.

Particle exchange move is performed in which one particle is removed from the selected box and added to a random location in the other box. The probability of acceptance, written here for transfer from box II to box I, is⁴⁹

$$P_{exc} = \min \left[1, \frac{N_{II}V_I}{(N_I + 1)V_{II}} \exp(-\beta\Delta U_I - \beta\Delta U_{II}) \right] \quad (14)$$

where N denotes number of particles, V is the volume, and ΔU is the configuration energy change resulting from the particle exchange.

The acceptance probability for a volume exchange move in which the volume of box I is increased by ΔV with the corresponding decrease of the volume of box II is,⁴⁹

$$P_{vol} = \min \left[1, \exp \left(-\beta\Delta U_I - \beta\Delta U_{II} + N_I \ln \frac{V_I + \Delta V}{V_I} + N_{II} \ln \frac{V_{II} - \Delta V}{V_{II}} \right) \right] \quad (15)$$

where ΔU is the configuration energy change resulting from the volume exchange. Implementation of eqs 13–15 and other technical details are described in the textbook by Frenkel and Smit.⁴⁹ In all GEMC simulations, we utilized 6×10^6 configurations, the first 4×10^6 configurations were discarded to guarantee equilibration.

The adsorption isotherms were computed by our grand canonical Monte Carlo code (GCMC).⁵⁰ In GCMC simulation of adsorption, configurational sampling of argon is carried out at a fixed chemical potential, temperature, and volume using three types of Monte Carlo moves: particle displacement, insertion of new particles into the pore volume, and deletion of particles from the pore volume.⁴⁹ Acceptance of displacement move is given by eq 13.⁴⁹ The insertion and deletion of randomly selected particles is accepted using the following equations:⁴⁹

$$P_{ins} = \min \left[1, \left(\frac{V}{N + 1} \right) \exp[\beta(\mu - \Delta U)] \right] \quad (16)$$

$$P_{del} = \min \left[1, \left(\frac{N}{V} \right) \exp[\beta(\Delta U - \mu)] \right] \quad (17)$$

where the μ is chemical potential and ΔU is the configuration energy change resulting from the particle insertion/deletion. Implementation of eqs 16 and 17 and other technical details are described in the textbook by Frenkel and Smit.⁴⁹

We used the previous setup for the GCMC simulation of adsorption in slit-shaped pore geometry, i.e., cuboidal simulation box $10\sigma_{ff} \times 10\sigma_{ff} \times H$ with periodic boundary conditions and minimum image convention for computing molecular interaction in x and y directions.³¹ The GCMC simulations utilized 2×10^8 configurations, the first 1×10^8

configurations were discarded to guarantee equilibration. We simulated 142 adsorption isotherms of argon at $T/T_c = 1.001$ and pressures from 1×10^{-14} to 4.6 MPa. All simulated adsorption isotherms of argon consisted of 321 points and covered the range of pore sizes, $H \in [0.23, 34]$ nm, where $H = H_{\text{geom}} - 0.34$ nm. The thermodynamic integration was performed according to eq 4 with an ideal gas as a reference state given by eq 5.

4. RESULTS AND DISCUSSION

4.1. Critical Point Parameters. The shape of the coexistence curve for argon obtained from the GEMC simulations is compared with the experimental data in Figure 1. The truncated LJ potential with effective dispersion

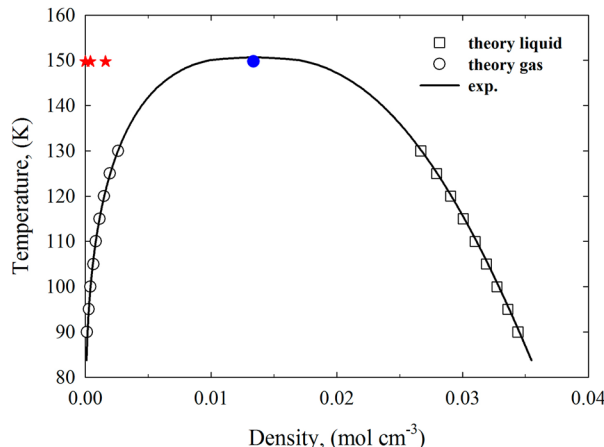


Figure 1. Experimental (solid line)⁵² and theoretical (open symbols) liquid–gas coexistence curves for argon. Theoretical critical parameters (i.e., closed circle: $T_c = 149.768$ K and $\rho_c = 0.0134$ mol/cm³) are in agreement with experimental data (i.e., $T_c = 150.687$ K and $\rho_c = 0.0134$ mol/cm³). Red stars indicate densities at $T/T_c = 1.001$ and pressures $p = 0.009, 0.48, 1.74$ MPa, respectively. The critical pressure of argon is 4.863 MPa.

parameters for argon reproduces the experimental measurements very well, including simulation data in the vicinity of the critical point. Very near the critical point, however, the simulation system cannot accommodate the long-range fluctuations. The simulation boxes switched the identity of the phases they contained, impacting the values of the collected thermodynamic averages. Therefore, we evaluated the critical parameters using the GEMC coexistence data collected in the vicinity of the critical point and the scaling relationships,^{24,51}

$$\frac{\rho_L + \rho_G}{2} = \rho_c + C(T_c - T) \quad (18)$$

$$\rho_L - \rho_G \propto (T_c - T)^\beta \quad (19)$$

where the liquid and gas densities of the coexisting phases, ρ_L and ρ_G , respectively, are determined from our series of the GEMC simulations. The critical temperature and density were evaluated by fitting eqs 18 and 19 to our GEMC simulation data collected at the vicinity of the critical point (see the work by Panagiotopoulos for other details⁵¹).

Our estimates of the critical parameters, $T_c = 149.768$ K and $\rho_c = 0.0134$ mol/cm³, are in very good agreement with the experimental data (i.e., $T_c = 150.687$ K and $\rho_c = 0.0134$ mol/cm³),⁵² as shown in Figure 1. For the same truncation of the LJ

potential, Panagiotopoulos reported $T_c = 153.464$ K and $\rho_c = 0.0135$ mol/cm³, which is close to but higher than our estimate.⁵¹ There can be several sources of this small discrepancy. Precise determination of the critical parameters is not a primary goal of our study. Small discrepancy can be explained by the extrapolation procedure or simulations details.

4.2. Solvation Pressures in Carbon Pores at Near-Critical Temperature. **4.2.1. Thin Pores.** The solvation force for $T/T_c = 1.001$ and pressures $p = 0.009, 0.48$, and 1.74 MPa is shown in Figure 2 (bottom panel) for pore widths $H < 1.2$ nm.

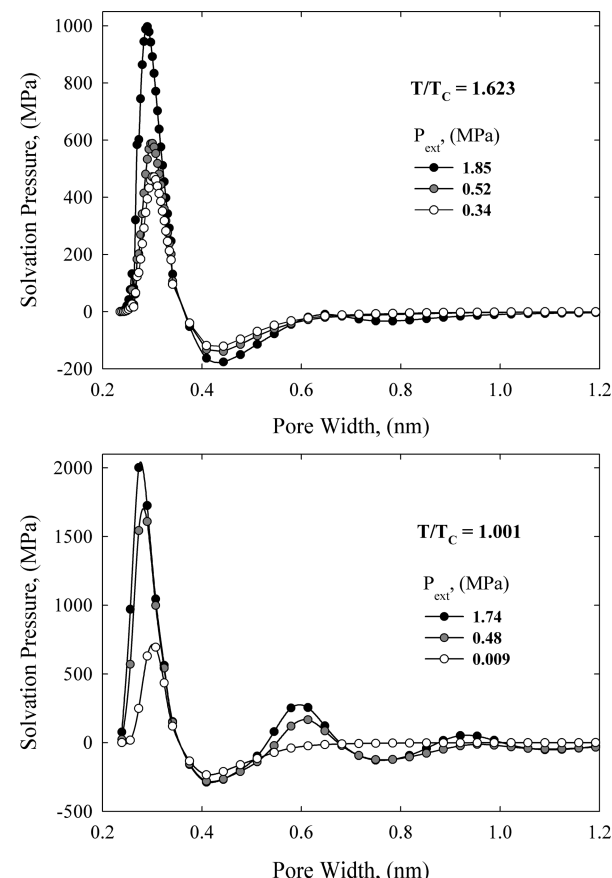


Figure 2. Solvation pressures of supercritical ($T/T_c = 1.623$)³¹ and near-critical ($T/T_c = 1.001$) argon versus slit-shaped carbon pore size. The corresponding bulk pressures are given on the plots. In swelling pores smaller than 0.38 nm, solvation pressures computed for near-critical argon adsorption are ~3 times larger than their values computed at supercritical temperature at near ambient pressures. Solvation pressures in carbon supermicropores ($0.7 < \text{pore size} < 2.0$ nm) are negligible at $T/T_c = 1.623$.

For comparison we show in Figure 2 (upper panel) the solvation force obtained in ref 31 for $T/T_c = 1.623$ and pressures $p = 0.34, 0.52$, and 1.85 MPa. The solvation force exhibits oscillatory decay for both the supercritical and the near-critical temperatures. The period of the oscillations, $\lambda \approx 0.33$ nm, and the positions of the extrema are almost the same in the two cases. The oscillatory decay follows from the packing effects - the force vanishes for optimal packing and is positive or negative if there is too little or too much space for the atoms between the surfaces. However, for the same external pressure the range and the magnitude of $f_s(H)$ are both much larger in the case of the near-critical argon than in the case of $T/T_c = 1.623$. The pressure must be decreased to 0.009 MPa at $T/T_c =$

1.001 to obtain similar $f_s(H)$ as for $T/T_c = 1.623$ and $p \approx 0.5$ MPa (see Figure 2). The larger amplitude can be explained by the larger density of the confined argon: the density increases by either decreasing T or by increasing p . In Figure 3, four

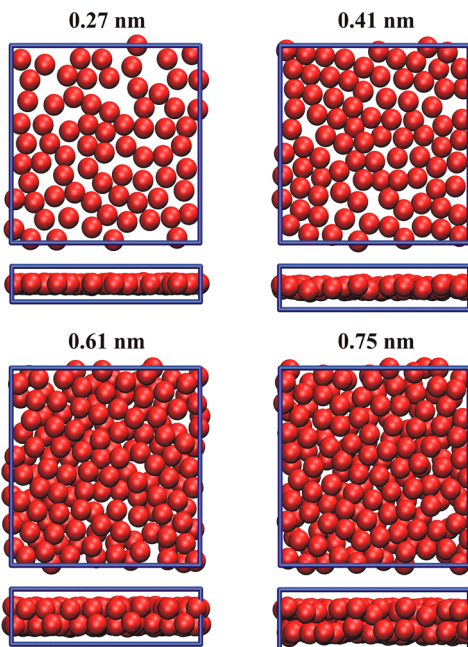


Figure 3. Equilibrium configurations of argon adsorbed in slit-shaped carbon pores at 4.56 MPa and $T/T_c = 1.001$. Pore widths are displayed on the top of snapshots.

snapshots of equilibrium configurations for the pore widths corresponding to one (top row) and two (bottom row) adsorbed layers are shown. In each case, two pore widths are selected, one corresponds to repulsion, and the other one to attraction between the confining surfaces.

4.2.2. Thick Pores. The results for larger range of pore widths and pressure in the range of $0.001 < p < 1.35$ MPa are shown in Figure 4. In the case of $T/T_c = 1.623$, the solvation force is negligible for $H > 1.0$ nm (see Figure 2), whereas for $T/T_c = 1.001$ it is significant for H up to 2 nm for the same range of pressures. For $H > 0.7$ nm, one can observe that the oscillations are superimposed on an attractive background. For a given range of subcritical pressures $p < p_0$, the force is attractive for $H > H_0(p_0)$, where $H_0(p_0)$ increases with increasing p_0 . This behavior is a clear indication of a tendency toward the predicted attraction of the Casimir force. At the same time, it shows that one needs really large widths H in order to observe the universal attractive force (eq 6) for the critical pressure.

There is another interesting feature of $f_s(H)$, namely, its dependence on p for fixed H . By inspection of $f_s(H)$ for $H = 0.95$ nm corresponding to geometrical compression (see Figure 5) one can see that for increasing p the solvation force first decreases, takes a minimum, increases again, and reaches positive values when the pressure increases beyond a certain H -dependent value. Similar behavior is repeated for different thickness corresponding to geometrical compression, $H = 0.95 + n \cdot 0.33$ nm (0.33 nm is the period of damped oscillations), but the force becomes positive for H -dependent pressure, which increases for increasing integer n . The dependence of $f_s(H)$ on p for several widths $1.8 \leq H \leq 5.1$ nm is shown in Figure 6. For

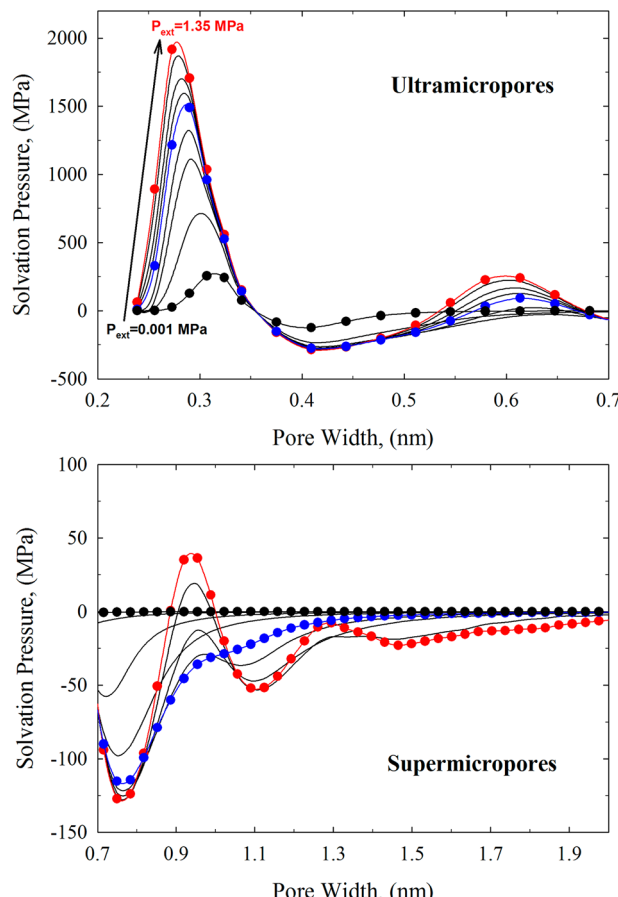


Figure 4. Solvation pressures of argon at $T/T_c = 1.001$ versus slit-shaped carbon pore size. Upper panel shows the region of ultramicropores (pore size < 0.7 nm), whereas the long-range attractive Casimir forces in supermicropores ($0.7 <$ pore size < 2.0 nm) are magnified in a bottom panel. Presented results covered the range of bulk pressures, $p_{\text{ext}} \in [0.001, 1.35]$ MPa.

such thickness we no longer observe repulsion up to $p = 4.6$ MPa. Note that, for increasing H , the positions of the minima of the solvation force move toward higher pressures, and the depth of the minima decreases. This behavior resembles the dependence of the Casimir force on $\mu - \mu_c$ predicted theoretically,⁴¹ and discussed in section 2.2. By inspection of the structure of the confined fluid, we did not observe any indication of phase transitions, in agreement with thermodynamic considerations.

We should note that our numerical procedures are not sufficiently accurate for pore widths ~ 5 nm and larger, and for weak forces. For this reason we do not try to consider $H > 5$ nm and $p = 4.6$ MPa. Nevertheless, our results for the intermediate range of H and p show how the nonuniversal oscillatory solvation force crosses over to the attractive Casimir force for increasing H .

4.3. Deformation of Activated Carbon Induced by Argon Adsorption at Near-Critical Temperature. The results of section 4.2 are used in this section for determination of the volumetric strain in porous material from eqs 3–5 and eqs 8 and 9 with the elastic constant and pore-size distribution determined in ref 31 for the supercritical argon at $T/T_c = 1.623$. We should stress that at $T/T_c = 1.623$ the solvation force for pores of widths $H > 0.8$ nm is negligible (see Figure 2). If such pores existed in the porous material, they could not be detected

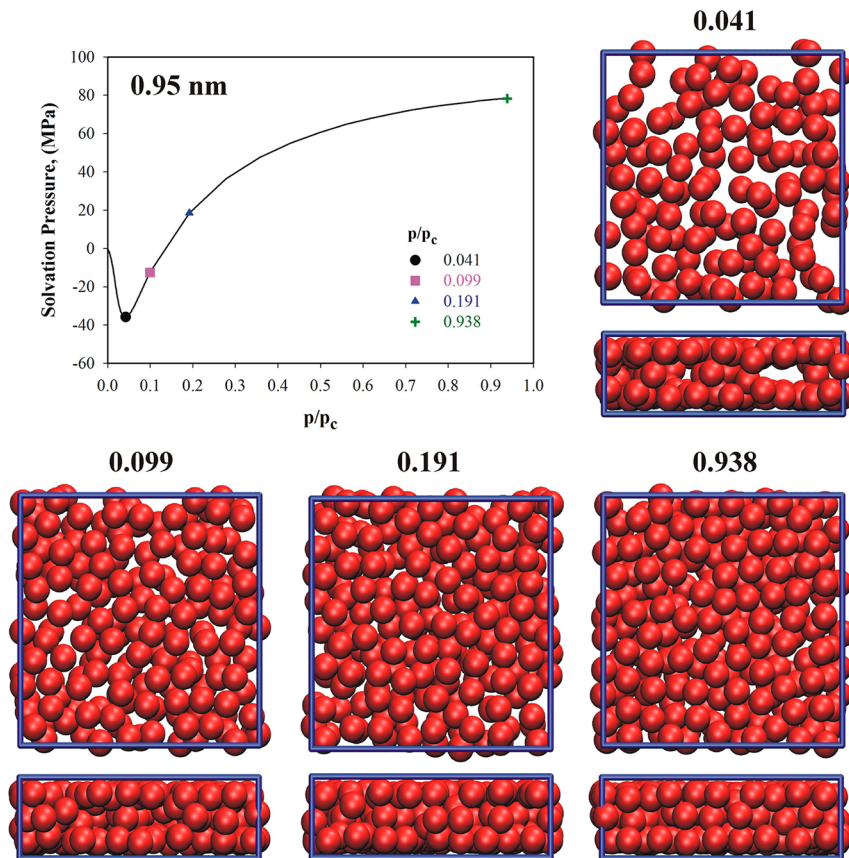


Figure 5. Equilibrium configurations of argon adsorbed in 0.95 nm supermicropore at 0.041, 0.099, 0.191, 0.938 p/p_c and $T/T_c = 1.001$.

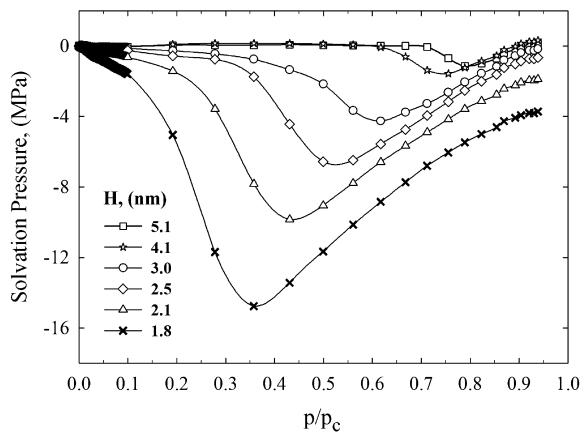


Figure 6. Solvation forces for several pore widths (region of supermicropores and narrow mesopores) as a function of p/p_c . The minims of solvation pressures are pore width-dependent and correspond to subcritical pressures.

by the present method at $T/T_c = 1.623$. Thus, the results of this section concern in fact a hypothetical porous material, containing only pores thinner than 0.8 nm. The volumetric strain predicted at $T/T_c = 1.001$ is shown in Figure 7 (right panel). For comparison, we show in Figure 7 (left panel) the results obtained in ref 31 at $T/T_c = 1.623$.

By fitting the experimentally measured volumetric strain to eq 9, it was found in ref 31 that $K = 7$ GPa, and the majority of pores have thickness of $H > 0.4$ nm. The solvation force for pores of widths ~ 0.4 nm is negative, and this leads to contraction of this material. The swelling observed for large

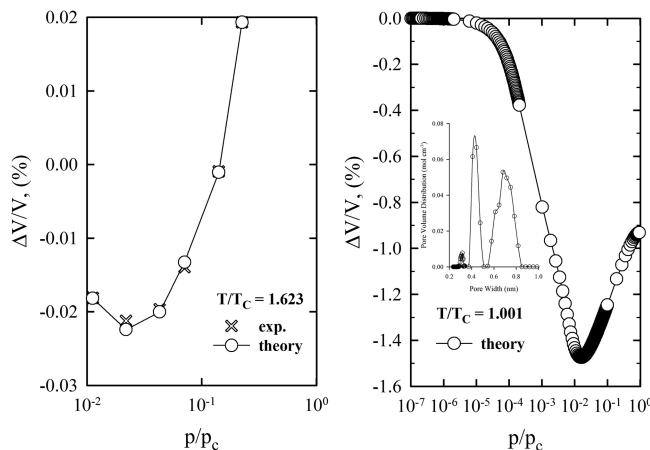


Figure 7. Left panel presents deformation of carbide-derived activated carbon upon supercritical argon adsorption (crosses: dilatometric experiment,⁵³ open circles: thermodynamic model³¹). Right panel shows theoretical prediction of dilatometric deformation curve for studied carbon sample (see embedded micropore size distribution) upon near-critical argon adsorption. Note that close to T_c , the initial contraction of activated carbon is 2 orders of magnitude greater than that experimentally measured at $T/T_c = 1.623$.

pressures follows from the significant increase of the repulsive solvation force for pores thinner than 0.4 nm and negligible increase of the attraction for $H > 0.4$ nm after increase of pressure. Similar asymmetry between the effect of increased pressure on the attractive and the repulsive solvation force is observed for $T/T_c = 1.001$ (Figure 2), and this leads to a similar trend in the volumetric strain as a function of pressure.

However, the initial contraction of porous sample is ~ 1.5 vol % (~ 2 orders of magnitude higher than at $T/T_c = 1.623$). Additional analysis performed for graphitic-like slit-shaped carbon pores modeled by 10–4–3 potential showed that initial contraction weakly depends on the thickness of carbon pore walls. Stronger contraction of slit-shaped graphitic pores (~ 2 vol %, as shown in Figure 1S in the Supporting Information) can be easily explained by deeper solid–fluid potential generated from infinitely long graphitic pore walls. Thus, the thickness of the carbon pore walls has no profound effect on the deformation of microporous carbons induced by near-critical argon adsorption. We should note that if in the studied material there exist pores with thickness $H > 0.8$ nm, the contraction of the porous material will be stronger than shown in Figure 7 (left panel), because the solvation force for such pores is attractive for the considered range of external pressures (see Figure 4).

5. SUMMARY AND CONCLUDING REMARKS

We have determined the solvation force for argon confined between carbon walls for near-critical temperature and a range of subcritical pressures. Based on these results, we computed the volumetric strain of a microporous carbon material with the elastic constant and the distribution of pore widths determined earlier.³¹

We have found that the solvation force has very similar properties in the near-critical and subcritical argon if the pore widths are $H < 0.8$ nm (i.e., in the range of carbon ultramicropores and narrow supermicropores). The strength of the force, however, in the case of the near-critical argon is 3 times larger at near ambient pressures. As a consequence, the volumetric strain in the same carbonaceous material is 2 orders of magnitude larger than at $T/T_c = 1.623$.

Significant differences between the confined near-critical and supercritical argon occur for pore widths $H > 0.8$ nm. While at $T/T_c = 1.623$ the solvation force is negligible, it is still quite strong at $T/T_c = 1.001$ for the considered range of subcritical pressures. For $H > 0.7$ nm the oscillatory solvation force is superimposed on an attractive background. For the pore widths corresponding to a geometric compression of the adsorbed argon, the external pressure must be sufficiently high to obtain repulsion between the walls. This external pressure increases with increasing number of the adsorbed layers of argon.

Previous results⁴¹ show that for fixed wall separation the Casimir force as a function of $h = \mu - \mu_c$ (see eq 6) is the strongest for some negative value of h , i.e., for some subcritical μ (or, equivalently, for subcritical pressure). The pressure corresponding to the strongest attraction for the fixed separation H increases with increasing H . Similar behavior was obtained here for the intermediate pore widths (see Figure 6). We conclude that the strongest stress occurs for the thermodynamic states that lie at the line emanating from the critical point of the capillary condensation, in analogy with the Widom line in the bulk system.⁴⁰

We limited our studies to the critical temperature of the bulk system, because we investigated a range of pore widths—the case relevant for porous materials. Temperature at the bulk critical point is higher than the critical point of the capillary condensation, and there are no phase transitions in the confined fluid. Thus, no additional physical effects influence the results. In the future, however, it would be interesting to consider a slit-shaped pore with a fixed width for a range of

temperatures and pressures, especially near the critical point of the capillary condensation.

The accuracy of our numerical procedure does not allow for an investigation of pores with $H > 5$ nm, and of weak forces. We can speculate, however, that the universal Casimir force can occur only for slit-shaped carbon pores of widths so large that the repulsion does not occur up to the critical pressure. Our results indicate that the above-described crossover between the short-range oscillatory decay and the long-range attractive Casimir force occurs for a large range of pore widths.

The properties of the solvation force for pore widths $0.8 < H < 5$ nm can have important consequences for the volumetric strain. Up to a certain pressure, all pores of widths $H > 0.8$ nm should be compressed (see Figure 4). If such pores are also present in the investigated carbonaceous material, then the compression of the sample is even larger than shown in Figure 7 (right panel).

Our results also indicate that the universal Casimir force could be observed in a porous material containing only pores of widths larger than ~ 10 nm. Although for typical microporous carbon the solvation force depends on the compressed fluid, we expect similar properties for different fluids in the pores of similar width in units of the molecular diameter, H/σ . This conjecture will be verified for near-critical CO₂ in our future studies.

■ ASSOCIATED CONTENT

S Supporting Information

Deformation of carbide-derived activated carbon upon near-critical argon adsorption is presented in Figure 1S. Here, the walls of slit-shaped carbon pores were modeled as infinitely long graphitic crystals. The 10–4–3 potential was used for calculations of solid–fluid potential energy. This material is available free of charge via the Internet at <http://pubs.acs.org>.

■ AUTHOR INFORMATION

Corresponding Author

*Tel: +61 8 9266 7800; E-mail: kowalczyk.piotr@wp.pl.

Notes

The authors declare no competing financial interest.

■ ACKNOWLEDGMENTS

The authors acknowledge Prof. Alexander V. Neimark (Rutgers University) for fruitful discussions and comments. A.C. acknowledges partial support by the NCN grant 2012/05/B/ST3/03302. P.K. acknowledges support by the Office of Research & Development, Murdoch University. P.K., A.P.T., P.A.G., and S.F. acknowledge the use of the computer cluster at Poznań Supercomputing and Networking Centre (Poznań, Poland) as well as the Information and Communication Technology Centre of the Nicolaus Copernicus University (Toruń, Poland). The authors thank Professor Leslie Glasser (Curtin University) for fruitful comments and suggestions.

■ REFERENCES

- Coudert, F.-X.; Boutin, A.; Fuchs, A. H.; Neimark, A. V. Adsorption Deformation and Structural Transitions in Metal-Organic Frameworks: From the Unit Cell to the Crystal. *J. Phys. Chem. Lett.* **2013**, *4*, 3198–3205.
- Kowalczyk, P.; Furmaniak, S.; Gauden, P. A.; Terzyk, A. P. Carbon Dioxide Adsorption-Induced Deformation of Macroporous Carbons. *J. Phys. Chem. C* **2010**, *114*, 5126–5133.

- (3) Brochard, L.; Vandamme, M.; Pellenq, R.-J.-M.; Fen-Chong, T. Adsorption-Induced Deformation of Microporous Materials: Coal Swelling Induced by CO₂-CH₄ Competitive Adsorption. *Langmuir* **2012**, *28*, 2659–2670.
- (4) Tvardovskiy, A. V. *Sorbent Deformation*; Elsevier Ltd.: Oxford, 2007.
- (5) Osborn, S. G.; Vengosh, A.; Warner, N. R.; Jackson, R. B. Methane Contamination of Drinking Water Accompanying Gas-Well Drilling and Hydraulic Fracturing. *Proc. Natl. Acad. Sci. U.S.A.* **2011**, *108*, 8172–8176.
- (6) Günther, G.; Prass, J.; Paris, O.; Schoen, M. Novel Insights into Nanopore Deformation Caused by Capillary Condensation. *Phys. Rev. Lett.* **2008**, *101*, 086104.
- (7) Gor, G.; Neimark, A. V. Adsorption-Induced Deformation of Mesoporous Solids. *Langmuir* **2010**, *26*, 13021–13027.
- (8) Blazer, Ch.; Wildhage, T.; Braxmeier, S.; Reichenauer, G.; Olivier, J. P. Deformation of Porous Carbon Upon Adsorption. *Langmuir* **2011**, *27*, 2553–2560.
- (9) Jeromenok, J.; Weber, J. Restricted Access: On the Nature of Adsorption/Desorption Hysteresis in Amorphous, Microporous Polymeric Materials. *Langmuir* **2013**, *29*, 12982–12989.
- (10) Kowalczyk, P.; Furmaniak, S.; Gauden, P. A.; Terzyk, A. P. Methane-Induced Deformation of Porous Carbons: From Normal to High-Pressure Operating Conditions. *J. Phys. Chem. C* **2012**, *116*, 1740–1747.
- (11) Poloni, R.; Lee, K.; Berger, R. F.; Smit, B.; Neaton, J. B. Understanding Trends in CO₂ Adsorption in Metal–Organic Frameworks with Open-Metal Sites. *J. Phys. Chem. Lett.* **2014**, *5*, 861–865.
- (12) Numaguchi, R.; Tanaka, H.; Watanabe, S.; Miyahara, M. T. Dependence of Adsorption-Induced Structural Transition on Framework Structure of Porous Coordination Polymers. *J. Chem. Phys.* **2014**, *140*, 044707.
- (13) Zang, J.; Nair, S.; Sholl, D. S. Osmotic Ensemble Method For Predicting Adsorption-Induced Structural Transitions in Nanoporous Materials Using Molecular Simulations. *J. Chem. Phys.* **2011**, *134*, 184103.
- (14) Boot-Handford, M. E.; Abanades, J. C.; Anthony, E. J.; Blunt, M. J.; Brandani, S.; Mac Dowell, N.; Fernandez, J. R.; Ferrari, M.-Ch.; Gross, R.; Hallett, J. P.; Haszeldine, R. S.; Heptonstall, P.; Lynbfelt, A.; Makuch, Z.; Mangan, E.; Porter, R. T. J.; Pourkashanian, M.; Rochelle, G. T.; Shah, N.; Yao, J. G.; Fennell, P. S. Carbon Capture and Storage Update. *Energy Environ. Sci.* **2014**, *7*, 130–189.
- (15) Scott, V.; Gilfillan, S.; Markusson, N.; Chalmers, H.; Haszeldine, R. S. Last Chance for Carbon Capture and Storage. *Nat. Clim. Change* **2013**, *3*, 105–111.
- (16) Grajek, H. Regeneration of Adsorbents by the Use of Liquid, Subcritical and Supercritical Carbon Dioxide. *Adsorpt. Sci. Technol.* **2000**, *18*, 347–371.
- (17) Israelachvili, J. N. *Intermolecular and Surface Forces*, 3rd ed.; Academic Press: Boston, 2011.
- (18) Evans, R. Fluids Adsorbed in Narrow Pores: Phase Equilibria and Structure. *J. Phys.: Condens. Matter* **1990**, *2*, 8989–9007.
- (19) Fisher, M. E.; de Gennes, P. G. *C. R. Acad. Sci., Ser. B* **1978**, *287*, 207–209.
- (20) Pousaneh, F.; Ciach, A.; Maciolek, A. Effect of Ions on Confined Near-Critical Binary Aqueous Mixture. *Soft Matter* **2012**, *8*, 7567–7581.
- (21) Ganshin, A.; Scheidemantel, S.; Garcia, R.; Chan, M. H. W. Critical Casimir Force in ⁴He Films: Confirmation of Finite-Size Scaling. *Phys. Rev. Lett.* **2006**, *97*, 075301.
- (22) Nguyen, Van D.; Faber, S.; Hu, Z.; Wegdam, G. H.; Schall, P. Controlling Colloidal Phase Transitions with Critical Casimir Forces. *Nat. Commun.* **2013**, *4*, 1584.
- (23) Hertlein, C.; Helden, L.; Gambassi, A.; Dietrich, S.; Bechinger, C. Direct Measurement of Critical Casimir Forces. *Nature* **2008**, *451*, 172–175.
- (24) Goldenfeld, N. *Lectures on Phase Transition and the Renormalization Group*; Westview Press: Oxford, 1992.
- (25) Evans, R. The Nature of the Liquid-Vapor Interface and Other Topics in the Statistical Mechanics of Non-Uniform, Classical Fluids. *Adv. Phys.* **1979**, *28*, 143–200.
- (26) Ravikovitch, P. I.; Vishnyakov, A.; Neimark, A. V. Density Functional Theories and Molecular Simulations of Adsorption and Phase Transitions in Nanopores. *Phys. Rev. E* **2001**, *64*, 011602.
- (27) Landers, J.; Gor, G. Yu.; Neimark, A. V. Density Functional Theory Methods for Characterization of Porous Materials. *Colloids Surf. A* **2013**, *437*, 3–32.
- (28) Bansal, R. Ch.; Goyal, M. *Activated Carbon Adsorption*; CRC Press: Boca Raton, FL, 2005.
- (29) Dubinin, M. M.; Kadlec, O.; Zukal, A. Carbon Adsorbents with Molecular Sieve Properties. *Nature* **1965**, *207*, 75–76.
- (30) Kowalczyk, P.; Gauden, P. A.; Terzyk, A. P.; Furmaniak, S. Microscopic Model of Carbonaceous Nanoporous Molecular Sieves-Anomalous Transport in Molecularly Confined Spaces. *Phys. Chem. Chem. Phys.* **2010**, *12*, 11351–11361.
- (31) Kowalczyk, P.; Ciach, A.; Neimark, A. V. Adsorption-Induced Deformation of Microporous Carbons: Pore Size Distribution Effect. *Langmuir* **2008**, *24*, 6603–6608.
- (32) Krech, M. Fluctuation-Induced Forces in Critical Fluids. *J. Phys.: Condens. Matter* **1999**, *11*, R391.
- (33) Brankov, G.; Tonchev, N. S. Danchev, D. M. *Theory of Critical Phenomena in Finite-Size Systems*; World Scientific: Singapore, 2000.
- (34) Krech, M.; Dietrich, S. Finite-Size Scaling For Critical Films. *Phys. Rev. Lett.* **1991**, *66*, 345–348.
- (35) Vasilyev, O.; Maciolek, A.; Dietrich, S. Critical Casimir Forces for Ising Films with Variable Boundary Fields. *Phys. Rev. E* **2011**, *84*, 041605.
- (36) Drzewinski, A.; Maciolek, A.; Ciach, A. Effect of Bulk Magnetic Field on Critical Ising Films. *Phys. Rev. E* **2000**, *61*, 5009–5018.
- (37) Pelissetto, A.; Vicari, E. Critical Phenomena and Renormalization-Group Theory. *Phys. Rep.* **2002**, *368*, 549–727.
- (38) Albano, E. V.; Binder, K.; Paul, W. Capillary condensation in the two-dimensional lattice gas: A Monte Carlo test of fluctuation corrections to the Kelvin equation. *J. Phys. A: Math. Gen.* **1997**, *30*, 3285–3297.
- (39) Simeoni, G. G.; Bryk, T.; Gorelli, F. A.; Krisch, M.; Rucco, G.; Santoro, M.; Scopigo, T. The Widom line as the crossover between liquid-like and gas-like behavior in supercritical fluids. *Nat. Phys.* **2010**, *6*, 503–5037.
- (40) Widom, B. Surface Tension of Fluids. In *Phase Transition and Critical Phenomena*; Domb, C., Green, M. S., Eds.; Academic Press: London, 1972, Vol. 2.
- (41) Drzewinski, A.; Maciolek, A.; Evans, R. Influence of Capillary Condensation on the Near-Critical Solvation Force. *Phys. Rev. Lett.* **2000**, *85*, 3079–3082.
- (42) Wang, Y.; Panzik, J. E.; Kiefer, B.; Lee, K. K. M. Crystal structure of graphite under room-temperature compression and decompression. *Sci. Rep.* **2012**, *2*, 5201–7.
- (43) Lennard-Jones, J. E. On the Determination of Molecular Fields. *Proc. R. Soc. London A* **1924**, *106*, 463–477.
- (44) Verlet, L. Computer “Experiments” on Classical Fluids. I. Thermodynamical Properties of Lennard-Jones Molecules. *Phys. Rev.* **1967**, *159*, 98–103.
- (45) Steele, W. A. *The Interaction of Gases with Solid Surfaces*; Pergamon Press: Oxford, 1974.
- (46) Kowalczyk, P.; Gauden, P. A.; Terzyk, A. P.; Neimark, A. V. Screening of Carbonaceous Nanoporous Materials for Capture of Nerve Agents. *Phys. Chem. Chem. Phys.* **2013**, *15*, 291–298.
- (47) Nguyen, Van T.; Horikawa, T.; Do, D. D.; Nicholson, D. On the Relative Strength of Adsorption of Gases on Carbon Surfaces with Functional Groups: Fluid–Fluid, Fluid–Graphite and Fluid–Functional Group Interactions. *Carbon* **2013**, *61*, 551–557.
- (48) Panagiotopoulos, A. Z. Direct Determination of Phase Coexistence Properties of Fluids by Monte Carlo Simulation in a New Ensemble. *Mol. Phys.* **1987**, *61*, 813–826.
- (49) Frenkel, D.; Smit, B. *Understanding Molecular Simulation from Algorithms to Applications*; Academic Press: London, 1996.

- (50) Kowalczyk, P.; Holyst, R.; Tanaka, H.; Kaneko, K. Distribution of Carbon Nanotube Sizes from Adsorption Measurements and Computer Simulation. *J. Phys. Chem. B* **2005**, *109*, 14659–14666.
- (51) Panagiotopoulos, A. Z. Direct Simulation of Fluid Phase Equilibria by Simulation in Gibbs Ensemble: A Review. *Mol. Simul.* **1992**, *9*, 1–23.
- (52) Stewart, R. B.; Jacobsen, R. T. Thermodynamic Properties of Argon from the Triple Point to 1200 K with Pressures to 1000 MPa. *J. Phys. Chem. Ref. Data* **1989**, *18*, 639–798.
- (53) Yakovlev, V. Yu; Fomkin, A. A.; Tvardovskiy, A. V.; Sinitsyn, V. A.; Pulin, A. L. *Russ. Chem. Bull.* **2003**, *52*, 354–358.